Article

Design and Optimization of Microfluidic Vortex Diode

Krzysztof Tadyszak *[ORCID], Alessandro Jäger, Jiří Pánek and Martin Hrubý [ORCID]

Institute of Macromolecular Chemistry, Czech Academy of Sciences, Heyrovského nám. 2,
162 06 Prague, Czech Republic; alejager@gmail.com (A.J.); panek@imc.cas.cz (J.P.); mhruby@centrum.cz (M.H.)
* Correspondence: tadyszak@imc.cas.cz

Abstract: The performed research presents modeling results for designing microfluidic vortex diodes. These devices rectify fluid flow and can be used in many applications on micro and macro scales. The modeling, utilizing computational fluid dynamics (CFD) with the turbulence model RANS k-ε in COMSOL Multiphysics, has led to optimizing diodicity—the reversed-to-forward flow pressure drop ratio. The goal was to find the best flow-rectifying geometry within the 2D vortex-type design by changing the wall geometry, diode shape, and inflow velocities, identifying significant parameters and dependencies. Improving diodicity can be achieved by increasing the radius r_1 of the central channel, increasing the entire diode radius r_2, decreasing the width w of the rectangular channel, and reducing its length L. Additionally, changing the circular shape of the diode to an elliptical one can improve diodicity. The significance of this research is evident in the potential applications of these devices in microfluidic setups where fixed-geometry unidirectional flow is required, e.g., mixing, filtration, cell separation, and drug delivery, or on industrial scales, e.g., energy harvesting, wastewater treatment, and water sterilization.

Keywords: fixed-geometry fluidic diode; fluidic check valve; unidirectional fluid flow; turbulent flow; RANS; computational fluid dynamics; COMSOL

1. Introduction

Fluidic diodes rectify the flow of fluid, e.g., gas or liquid. This unidirectional flow can be further utilized in the following stages [1,2]. Microfluidic chips can be used in bio/medical applications [3,4], e.g., cell separation [5], obtaining particles for drug delivery [5–9], mixing [10–13], and micro-pumping [14,15], or in industrial scales, e.g., turbines [16], or heat pumping [17,18], heat removal [19], wastewater treatment [20–24], bacteria removal [25], and chemical reactions under hydrodynamic cavitation conditions [26–30], or in larger-scale applications, e.g., a passive safety system in a molten salt reactor [31], energy harvesting [32–35], or ventilation purposes [36]. Fluidic diodes can be separated into two groups: passive and active. The first has no movable parts; the flow-rectifying effect is only achieved due to geometry. In active design, the movable part blocks the reverse flow and opens during the forward flow. Usually, active diodes, due to the changeable geometry, can outperform the passive valves up to the moment the movable part is even slightly blocked or corroded and cannot close the flow [37].

This article focuses on a particular type of passive diode in the shape of a disc (vortex-type fluidic diode) [38–40]. Although vortex diodes are 3D devices, their general characteristics can be modeled using a simplified 2D design, avoiding high computational costs. In the case of thin 3D channels, which can be found in microfluidic applications, a 2D model only approximates real-life devices [40].

This article presents no previously shown geometrical modifications to increase diodicity in microfluidic vortex diodes. All this is performed for small fluid velocities and volumes, translating to small Reynolds numbers (Re). Modeling large Re numbers and larger fluid volumes has been performed elsewhere [38,39]. The RANS k-ε model applied here was previously used to model the influence of the angle of the axial port of 3D vortex

diodes [41–44], cavitation [45,46], water hammer effects in vortex diodes [47], and while modeling flows in microfluidic chips [48,49]. Diodicity improvement in this article was achieved only by utilizing geometrical changes without influencing the physical properties of the walls, channels, and fluid. It was shown that improvement is possible by increasing the size of the central channel and the entire diode, reducing the width of the rectangular side channel and its length, or changing the shape from circular to elliptical for specific cases. The goal was to find a straightforward design that outperforms plain circular diodes and is readily applicable to photolithography.

2. Model and Parameters

Computational fluid dynamics (CFD) modeling using the Fluid Flow Module with the *Turbulent flow k-ε* model with the COMSOL ver. 5.6.0.401 program was used to model the properties of microfluidic vortex diodes [41]. The program utilizes Reynolds-averaged Navier–Stokes (RANS) equations, a simplified set of equations used to describe the average behavior of fluid flows [50–52] (Table 1). The turbulent kinetic energy k and the turbulent dissipation rate ε are introduced to describe the turbulence behavior. The turbulent viscosity is modeled as follows:

$$\mu_T = \rho C_\mu \frac{k^2}{\varepsilon}. \tag{1}$$

Table 1. List of symbols used in the article.

p_{in}, p_{out}	Pressure at flow entry and exit
D	Diodicity
Re, L_c, μ	Reynolds number, characteristic length, fluid dynamic viscosity
r_1	The radius of the circular, central channel
$l(r_1)$	Circumference of the circular channel
$\boldsymbol{u}, v_{in}, v_{out}$	Flow velocity vector, inflow velocity, outflow velocity
L, w	Length and width of rectangular channel
r_2	Diode radius
α	The general rotation angle of specific detail
A	The base length of the triangle, tooth element
h	The height of the triangle, tooth element
$\Delta P_{rev.}/\Delta P_{forv.}$	Difference in pressures—applied and at the end of the diode in the reversed/forward flow direction
μ_T	Turbulent viscosity
C, σ, P_k	Model constants, production term
ρ	Fluid density
k, ε	Turbulent kinetic energy, turbulent dissipation rate

The transport equations for k and ε are as follows:

$$\rho \frac{\partial k}{\partial t} + \rho \boldsymbol{u} \cdot \nabla k = \nabla \cdot \left(\left(\mu + \frac{\mu_T}{\sigma_k} \right) \nabla k \right) + P_k - \rho\varepsilon, \text{ where} \tag{2}$$

$$P_k = \mu_T \left(\nabla \mathbf{u} : \left(\nabla \mathbf{u} + (\nabla \mathbf{u})^T \right) - \frac{2}{3}(\nabla \cdot \mathbf{u})^2 \right) - \frac{2}{3}\rho k \nabla \cdot \mathbf{u} \tag{3}$$

$$\rho \frac{\partial \varepsilon}{\partial t} + \rho \boldsymbol{u} \cdot \nabla \varepsilon = \nabla \cdot \left(\left(\mu + \frac{\mu_T}{\sigma_\varepsilon} \right) \nabla \varepsilon \right) + C_{\varepsilon 1} \frac{\varepsilon}{k} P_k - C_{\varepsilon 2} \rho \frac{\varepsilon^2}{k}, \tag{4}$$

with constants $C_\mu = 0.09$, $C_{\varepsilon 1} = 1.44$, $C_{\varepsilon 2} = 1.92$, $\sigma_k = 1.0$, and $\sigma_\varepsilon = 1.3$, where $\mathbf{u}$ is the velocity vector, $\rho = 998$ kg/m^3, and dynamic viscosity $\mu = 1.0016$ mPa·s of

water at 20 °C (Table 1). The vortex diode (Figure 1) consists of a large circle of radius r_2 = 100 μm (default), and a side rectangular arm of length L = 100 μm (default), and width w (act as input/output). The central channel part is a circle of radius r_1= 5 μm (default), and length $l = 2\pi r_1$ (acts as output/input). To maximize diodicity (D), which is defined as the ratio of the pressure difference at the source (p_{in}), and drain channel (p_{out}) in the reverse flow direction

$$\Delta P_{rev.} = p_{in} - p_{out} \tag{5}$$

to the same difference in the forward flow direction

$$D = \frac{\Delta P_{rev.}}{\Delta P_{forv.}} = \frac{(p_{in} - p_{out})_{rev.}}{(p_{in} - p_{out})_{forv.}}. \tag{6}$$
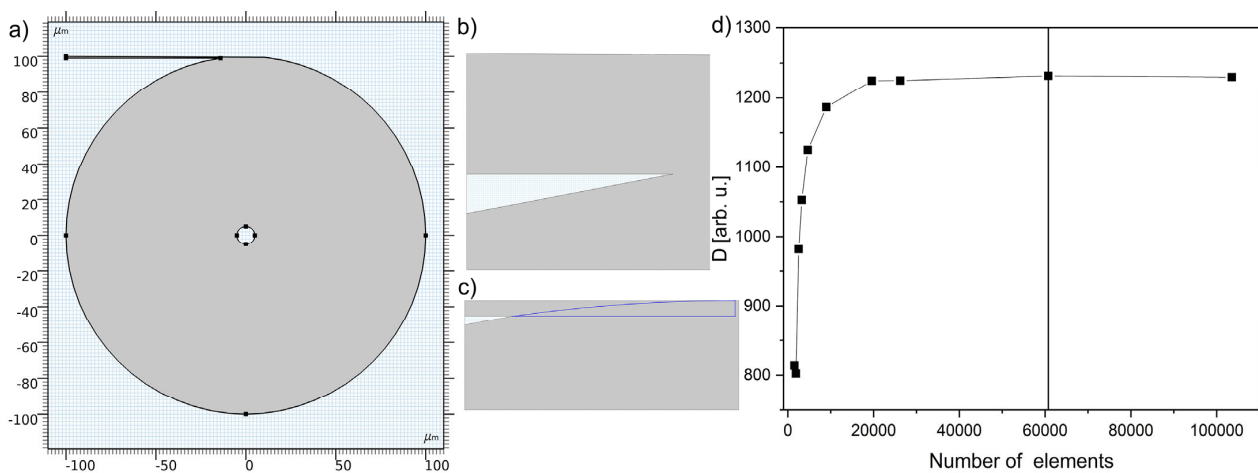
Figure 1. (**a**) Plain 2D model of the diode. The diode radius r_2 is 100 μm, the circular channel radius r_1 is 5 μm, the rectangular channel width w is 1 μm, and the length L is 100 μm; (**b**) magnification of the connection of rectangular channel with the diode; (**c**) the same magnification showing ignored edges; (**d**) diodicity D vs. the number of mesh elements. Mesh with 60,745 elements was used with $D = 1231$.

The pressures $p_{in./out.}$ were taken as the integrated fourth order polynomial span overall mesh nodes from both channels represented by the width w and the length $l = 2\pi r_1$. Many parameters, e.g., w, r_1, r_2, L, v_{in}, and geometrical changes, are tested to find their importance for improving diodicity.

The maximal Reynolds number (Re) for applied velocities does not exceed 100. It is lower in the forward direction, ca. 6.5, and ca. 73 in the reversed direction for plain geometry (default shape Figure 1). Re is a dimensionless indicator of turbulence in fluid dynamics, measuring the ratio between inertial and viscous forces. It is defined as follows:

$$Re = \frac{\rho v_{in} L_c}{\mu}, \tag{7}$$

where ρ is the fluid density, v_{in} is the flow speed, L_c is the characteristic length, and μ is the fluid dynamic viscosity. The basic version of the model is shown in Figure 1a. It comprises three elements: a large circle is the diode body, a small circle acts as a channel (subtracted from the diode body), and a rectangular channel is on top. Figure 1b,c show the connection of the rectangular channel with the diode. Marked blue lines refer to edges that the program ignored during computations. The extremely fine mesh calibrated for the fluid dynamics of triangular-shaped elements was used. The average mesh quality is 0.8831 (a value of 1 is perfect), the number of elements is 60745, and the minimum/maximum element sizes are 0.004/1.34 μm.

3. Results and Discussion

The vortex diode exhibits the advantages of passive diodes—no movable parts—and, compared to passive check-valve diodes, shows much higher *D*. Figure 2 presents the velocity maps and streamlines for the forward and reversed flow directions. The white velocity arrows inside and black at the rectangular channel entrance marked as v_{in}, v_{out} indicate the flow direction in both cases. The forward direction is characterized by a much lower pressure drop $\Delta P_{forv.}$ and *Re* number than the reversed one.
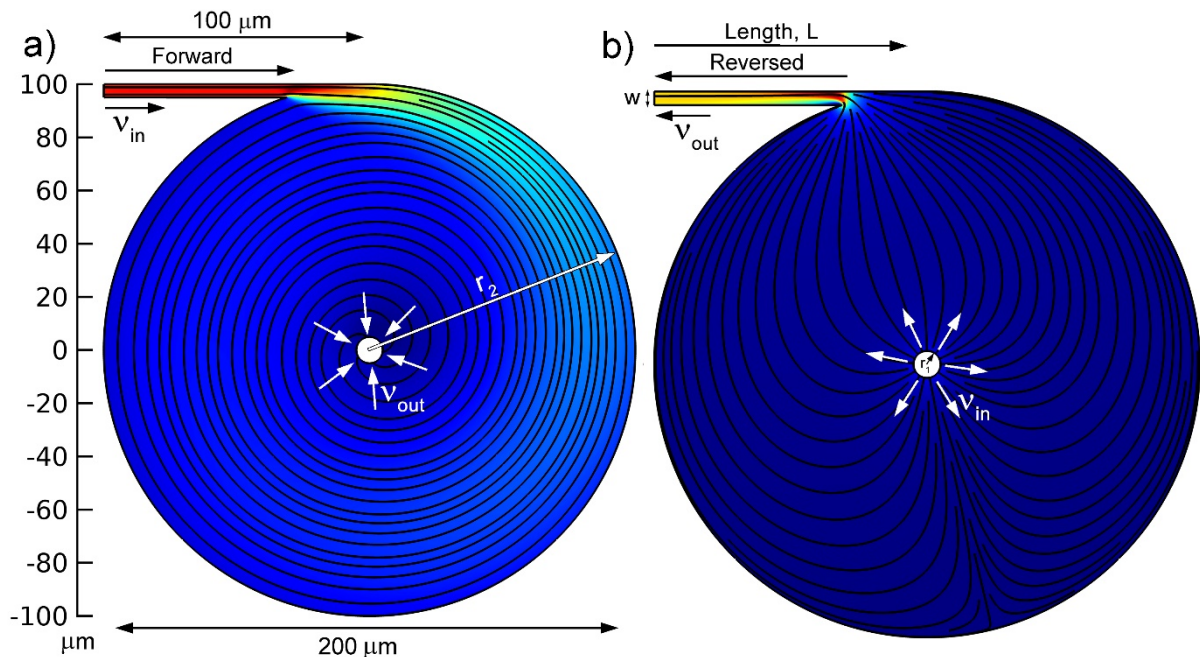
Figure 2. Two-dimensional models of vortex diodes; maps of velocity magnitude with streamlines (w—width of the rectangular channel (default vale 1 μm), *L*—length of rectangular channel (default value 100 μm), r_1—radius of the central channel (default value 5 μm), r_2—radius of the diode (default value 100 μm): (**a**) forward flow direction—inflow from side channel outflow in the center; (**b**) reversed flow direction—inflow from center circle outflow by the side channel.

It is assumed that the most significant influence on diodicity should arrive from both channel geometries and the size of the entire diode. This study starts with an investigation of this hypothesis. The defined parameters are the rectangular channel width w (source in the forward direction, Figure 2a) and the circumference of the circular channel $l(r_1) = 2\pi r_1$ (drain in forward direction, Figure 2a) addressed in this article through radius r_1 (Figure 2b). The pressure difference also depends on the velocity v_{in}, an additional parameter to be optimized. The diode consists of a large circle of radius $r_2 = 100$ μm and a side arm of length $L = 100$ μm with channel width $w = 1$ μm (Figure 2a). In the middle of the diode is a circular channel $l(r_1)$ (Figure 2a) of the radius $r_1 = 5$ μm (default value). The roles of the source and drain are reversible (Figure 2a,b).

Essential dependence on diodicity $D = f(r_1, w, v_{in})$ was found due to a parametric sweep through 3D space. The highest value is depicted in red (Figure 3a). The diodicity increases with channel width w decreasing, circular channel radius r_1, and velocity v_{in} increasing (Figure 3a). However, due to the manufacturing process, some limitations justify using a narrower parameter range—the lower limit of w is ca. 100 nm. The maximum size of r_1 is slightly lower than the diameter of the external wall, which, by default, is 200 μm. The parameters analyzed here are achievable experimentally in microfluidic devices. Figure 3b shows the dependence $D = f(v_{in})$, with channel width w ranging from 0.1 to 4 μm for fixed circular channel radius $r_1 = 20$ μm. The plot shows a flat maximum, which is better recognizable for smaller w values. The smallest w value equal

to 100 nm gives D, which reaches ca. 1.04×10^6 at 6 m/s. The inset shows a similar dependence of diodicity concerning velocity for multiple r_1 parameters in the range of 10–95 μm for channel width $w = 1$ μm. The inclusive maximum of plots appears for the velocity range 10–20 m/s, which shifts to higher velocities for larger r_1 values (Figure 3b, inset). The following plot is obtained from these data—maximal diodicity vs. channel width w (Figure 3c)—and the inset shows the velocity at maximum diodicity vs. channel width w. This dependence can be described by a power function of the type $y = aw^b$, where $a = 1.33 \times 10^4$, $b = -1.895$, $R^2 = 0.9997$ (fit made for $r_1 = 20$ μm, $v = 10$ m/s). Figure 3d shows diodicity vs. the radius of the circular channel r_1. This dependence can be described using the same function $y = ar_1^b$, where $a = 44.4$, $b = 1.97$, $R^2 = 0.9993$ (fit made for $w = 1$ μm, $v_{in} = 10$ m/s). If r_1 exceeds 97 μm, the curve gets much steeper and cannot be described with the above equation (case not shown here). The results show that diodicity is at least a three-parameter function—dependent on two channel widths and velocity.
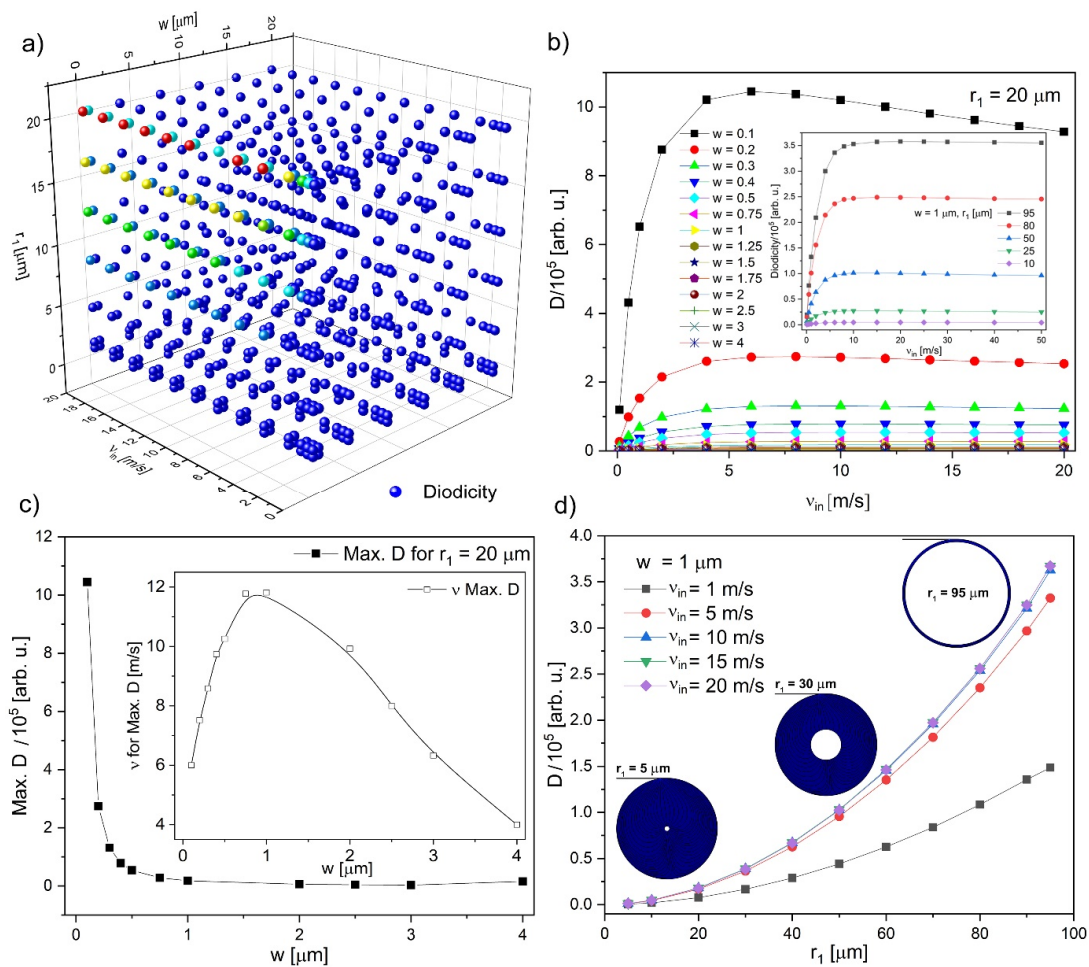
Figure 3. (**a**) Parametric sweep through 3D space, diodicity $D = f(r_1, w, v_{in})$. The color overlay shows diodicity D (red—highest, and blue—lowest value); (**b**) D vs. velocity for fixed radius $r_1 = 20$ μm for multiple channel widths w. The inset shows D vs. velocity for fixed channel width w = 1 μm and multiple radiuses r_1; (**c**) Max. D vs. channel width w for $r_1 = 20$ μm, inset shows maximal velocity v taken from function's maximum in Figure 3b vs. its channel width w; (**d**) D vs. channel radius r_1 for fixed channel width $w = 1$ μm and multiple velocities v_{in}. Inset shows images of the diodes with radius $r_1 = 5$ μm, $r_1 = 30$ μm, $r_1 = 95$ μm.

Figure 3a,b show the dependence on channel length L and radius r_2, respectively. The decrease in channel length L increases diodicity. For a diode of diameter 200 μm,

the minimal length of L is ca. 15 µm. Below this value, the rectangular channel connects with the main diode body, and the width w is no longer defined. For purely practical reasons, if a square is prepared on a microfluidic chip for a diode of radius 100 µm, then the longest justified length L cannot be larger than this in order to not exceed the square size, which is set as default. The dependence in Figure 4a can be well described by the empirical equation of the form $y = \frac{A}{L} + B$, where $A = 2.9 \times 10^4$, $B = 9.3 \times 10^3$, $R^2 = 0.9939$. The second parameter, r_2 is, affecting the technological process even more by increasing the total diode size—area (in 3D volume)—with an increase in r_2 (Figure 4b). All other parameters were kept constant, and the dependence can be fit with a polynomial of third order $y = A + Br_2 + Cr_2^2 + Dr_2^3$, where $A = 1.2 \times 10^3, B = 1.63, C = -6.1 \times 10^{-3}, D = 7.8 \times 10^{-6} \ R^2 = 0.9957$.
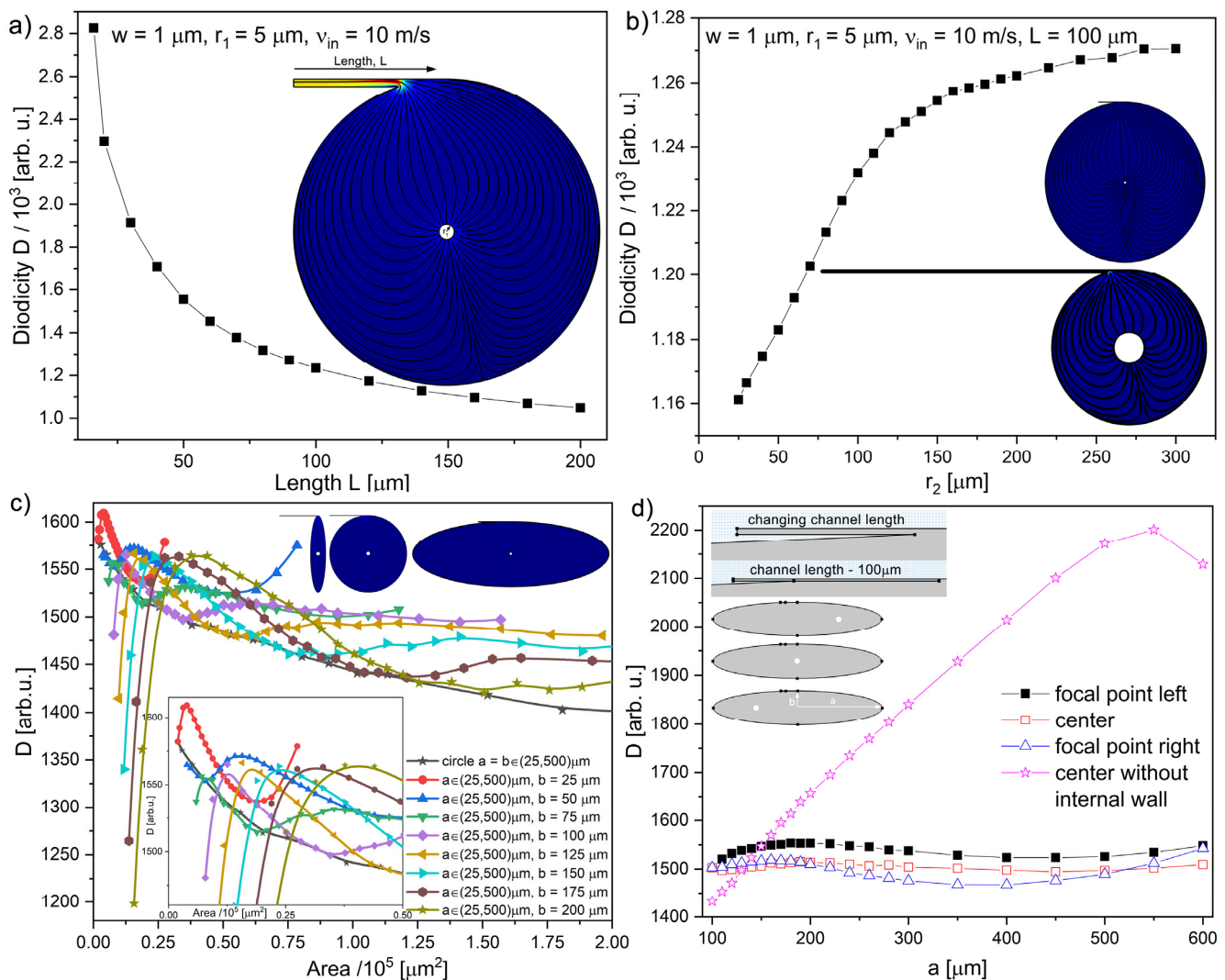
Figure 4. (**a**) Diodicity D vs. length L of the rectangular channel and (**b**) D vs. r_2 radius for $L = 100$ µm; (**c**) D vs. area of the diode for increased eccentricity (ellipse shape), where inset is the magnification of the main plot and additionally on top are the main ellipse shapes ($v_{in} = 10$ m/s); (**d**) D vs. horizontal radius a for central and focal placement of circular channel (left and right), for fixed vertical radius $b = 100$ µm, and fixed and varying L ($v_{in} = 10$ m/s).

Figure 3c shows the influence of increasing eccentricity (horizontal direction is radius a, while vertical radius b is a family parameter) on diodicity. To compare it with the circular case, the diodes are plotted as a function of the diode area. If the diode's shape and size were changed, the rectangular channel sticking out would differ each time. The internal wall

(Figure 3d, top inset) kept the rectangular channel length—*L*—equal to 100 µm, varying proportions between the inside and outside parts.

Elliptical shapes exhibit diodicity maxima, which are more diffuse for larger b values. Only the circular shape shows a monotonically decreasing diodicity similar to the curve in Figure 4a. The maximal improvement of *D* is 7.2% (blue curve *a* = 500, *b* = 50) compared to 4.6% (dark yellow curve *a* = 60, *b* = 200) for the circular diode shape (normalization factor-area). Figure 4d compares placing the circular channel in the center or the focal points for the ellipse (radius *a* = 100–600 µm and *b* = 100 µm); and for *L* = 100 µm (constant) and floating (without internal wall, marked by stars), for which the rectangular channel length shortens. Diodicity is slightly more significant for the circular channel in the left focal point (clockwise water rotation in forward direction, Figure 2a). In the case of the floating channel length (without an internal wall), diodicity increases linearly with radius a by ca. 32%. This effect is connected with a decrease in channel length *L*, similar to the case in Figure 4a where the outside part of the rectangular channel is decreased and does not change diode shape.

3.1. Wall Modifications

This chapter is focused on further wall-shape modifications to improve diodicity. The most straightforward wall modification is to change wall roughness or hydrophilicity. This could be performed experimentally by covering the diode from the inside with polymers or silanes. Nevertheless, this study focuses on geometrical changes that fundamentally improve diodicity. The basic structure is characterized by the following parameters: r_1 = 5 µm, w = 1 µm, v_{in} = 10 m/s, r_2 = 100 µm, and *L* = 100 µm with a default diodicity value of 1231. The first wall modification is adding a triangle-type obstacle (Figure 5a). Initially, it is a single triangle defined by three parameters *a*, *h*, and α = 0 (Figure 5a). The base of the triangle is *a* = 20 µm, and height h after an initial parametric sweep (Figure 5b, black curve) is set to 20 µm, which is for the maximum of *D*. The second stage is the placement of a single triangle obstacle at different angle α. The clockwise rotation goes from 0 to negative 340°.

The top placement of the triangle obstacle (α = 0, Figure 5b) provides the highest diodicity due to the most significant influence on the flow from the rectangular channel. Results for other angles are inferior. The next stage is to add symmetrically *N* identical triangles (Figure 5c). The first triangle always starts at α = 0. The observed outcome is the decrease in diodicity (Figure 5d). Further trials were continued with an asymmetrical tooth, which, from the left side, had a shape based on a quarter of an ellipsis and from another straight vertical line. The base width is *a* = 10 µm. Similarly, as before, the highest *D* is observed for tooth height *h* = 20 µm (Figure 6, black squares). No changes in diodicity were observed during the rotation of a single tooth (Figure 6, inset). Open squares in Figure 6 show a case for *N* = 13 teeth symmetrically placed on the wall. Diodicity for this case is also lower than previously. The wall modifications proposed here do not seem to improve *D*. The slight changes in *D* by ca. 1.3% compared to a plain diode (*D* = 1231) do not justify additional manufacturing difficulties. The lack of obstacles on the wall seems to be the most straightforward and well-working design from all tested until now.
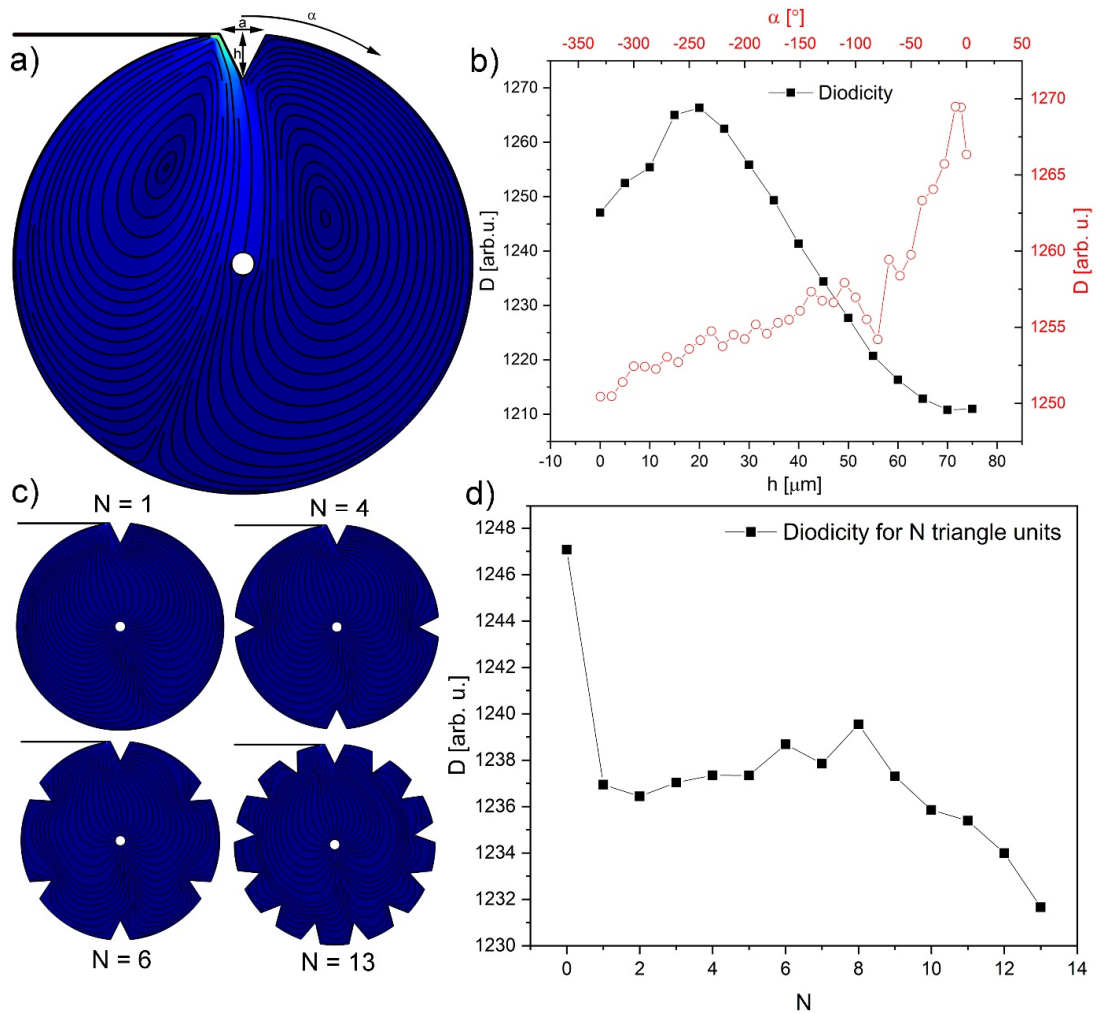
Figure 5. (**a**) Vortex diode with single triangle-shaped wall modification: height *h* = 20 μm, *a* = 20 μm, *α*—rotation angle, *w* = 1, r_1 = 5 μm; (**b**) *D* vs. *h* and *α* for single triangle rotation; (**c**) model with multiple triangles separated by the same angle; (**d**) *D* vs. *N*—number of repetitions *N* in range of 0 to 13.
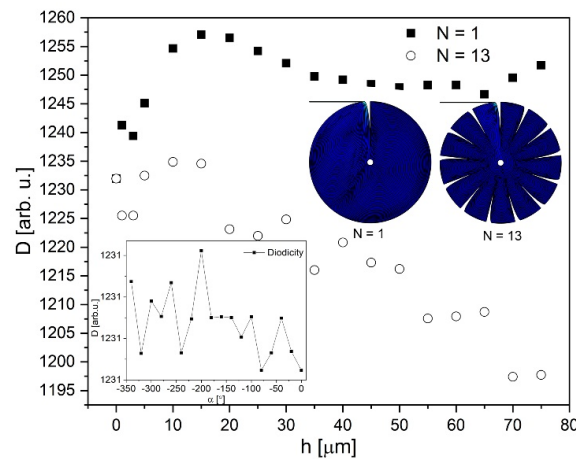
Figure 6. Diodicity *D* vs. height (*h*) of the elliptically shaped tooth (base width *a* = 10 μm) for single tooth *N* = 1 (black squares) and *N* = 13 (open circles). Images of two models are shown for *N* = 1 and *N* = 13 teeth. The inset plot shows diodicity vs. rotation angle *α* for a single tooth (*N* = 1).

3.2. Internal Structure Modification

Different types of modifications are structures placed inside the diode. Multiple types of internal wall design and channel geometries are presented in Figure 7a. The results for specific models are presented in Figure 7c. Figure 7a, cases a–c present various types of rectangular channel elongation inside the diode. In these cases, diodicity decreases (Figure 7c); case d shows the rectangular channel angle change from 0 to 90° from a tangential to perpendicular position. In this case, diodicity is highest for tangential channel orientation, consistent with the basic design of a vortex diode. Cases e and f show the application of an airfoil profile. Its shape is based on a symmetrical four-digit NACA airfoil (0050) equation $y = -5t \left(0.2969\sqrt{x} - 0.1260x - 0.3516x^2 + 0.2843x^3 - 0.1015x^4\right)$ for $t = 50$. The rotation of a single blade (Figure 7c) and after introducing more profiles, $N = 13$, (Figure 7b) shows small fluctuations in D but, generally, changes are minor, ca. 1.3%, and angle-dependent. In general, diodicity is more or less constant at ca. 1231, with a maximum for $N = 13$ equal to 1260.
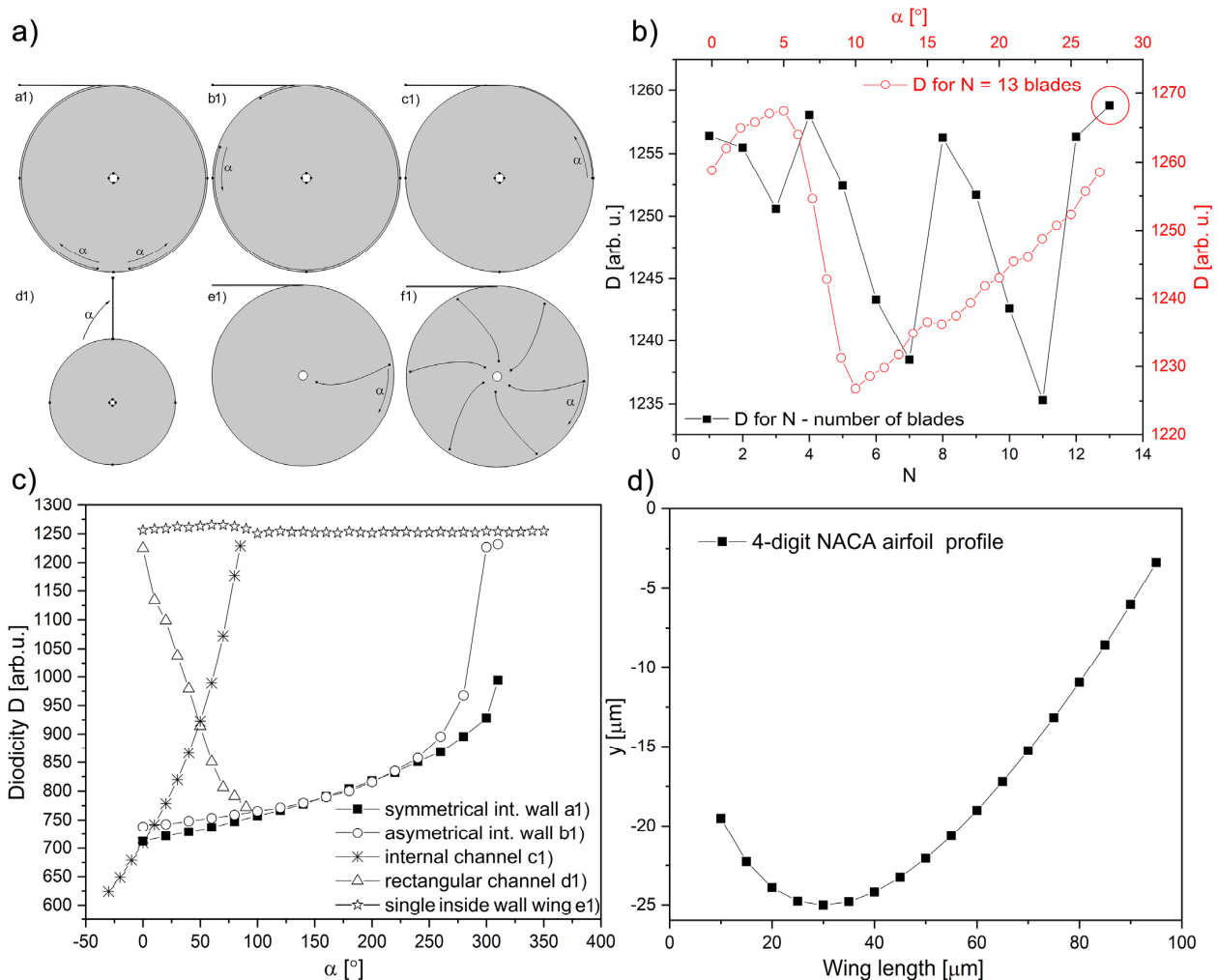
Figure 7. (**a**) Vortex diode design cases: (**a1**)—internal channel (width 2 μm) symmetrically reduced with the increase in α; (**b1**)—internal channel (width 2 μm) reduced with the increase in α in one direction, (**c1**)—internal channel (width 1 μm, continuation of external rectangular channel); (**d1**)—external channel change from 0 (tangential) to 90° (perpendicular direction); (**e1**)—single airfoil profile—internal wall; (**f1**)—13 airfoil profiles; (**b**) D vs. N—number of airfoil profiles (black squares) and D vs. 13 with profile angle α (open red circles); (**c**) angular diodicity dependence for all cases from Figure 7a; (**d**) airfoil profile drawn in the range 15–95 μm used as blades in cases (**e1,f1**).

Similarly, as in the outer wall modifications proposed, the internal wall obstacles did not improve diodicity significantly. The best improvement is by ca. 1.3%, which introduces an angular dependence that, if not considered, can decrease diodicity even below the plain diode performance. Introducing new geometry is always connected with locking some of the parameters while following the dependencies of selected ones, leaving some space for further improvements. Most ideas presented here generally maintained or decreased diodicity, except for elliptical elongation, which significantly improved by 7.2%. All this suggests that the circular/elliptical plain design is close to its optimal performance.

4. Conclusions

The passive vortex diode exhibits a better diodicity performance than a check-valve diode. Diodicity is a function of several geometrical parameters, i.e., r_1, r_2, w, L, and velocity v_{in} ($D = f(r_1, r_2, w, L, v_{in})$). The best improvement in diodicity in plain vortex diodes was achieved by an increase in radius r_1 of the central channel, an increase in the entire diode radius r_2, a decrease in width w of the rectangular channel, and a reduction in its length L or changing the circular shape of the diode to elliptical if the area is taken as the normalization factor for comparison with circular diodes. Other tested wall modifications on the outside or inside diode led to roughly maintaining diodicity as in the plain design or decreasing it.

The statements mentioned above are presented below in detail. The decrease in channel width w from 1 μm (default) to 0.1 μm increased D (1231 by default) by ca. 853 times (Figure 3b) for a specific velocity $v_{in} \approx 6$ m/s. Reduced rectangular channel length L from an initial 100 to 15 μm improves D 2.3 times (Figure 4a). The increase in r_1 from 5 to 95 μm improves D by ca. 285 times (Figure 3d). The result increases with v_{in}. It is highest for 20 m/s, the highest tested velocity. However, the difference in D between cases $v_{in} = 10$ and 20 m/s, which seems less significant than changes for smaller velocities. Saturation behavior is visible. The increase in diode size r_2 from 100 to 300 μm improved D only slightly, by ca. 2.9% (Figure 4b). Changes in the circular shape of the diode to elliptical improved D by ca. 1.3 times (Figure 4c). Changing the diode size diodicity depends on the definition of channel length L: it can merge with the diode body or exist as an internal wall of the diode (Figure 4d, inset). Diodicity is higher by ca. 32% in the case without an internal wall, similar to the case of the shortening of L.

Adding a wall results in slight changes in diodicity, which starts to be dependent on the height of the obstacle and the angle, e.g., triangles (Figure 5)—maximum D for height $h = 20$ μm, an increase by ca. 1.3%, and angle dependence vary this value by ca. 1.6%. The symmetrical placement of more obstacles, e.g., triangles, decreases diodicity by ca. 1.2% (Figure 5c,d) and elliptically shaped teeth by 3.3% (Figure 6).

Placing additional internal walls in the shape of airfoil profiles (Figure 7) led to a decrease in diodicity by 2.2% and an additional angle dependence (Figure 7b). Other proposed internal wall modifications presented in Figure 7a led to an even 49% drop in diodicity. The horizontal placement of the rectangular channel on top of the diode ($\alpha = 0°$) is the optimum placement of this channel. Placing it vertically to the diode ($\alpha = 90°$) decreases D by ca. 37%.

Author Contributions: For this research, authors participated in the following manner: conceptualization, K.T. and M.H.; methodology, K.T. and M.H.; validation, K.T. and M.H.; formal analysis, K.T.; investigation, K.T. and A.J.; data curation, K.T. and A.J.; writing—original draft preparation, K.T. and A.J.; writing—review and editing, K.T., J.P., M.H.; visualization, K.T. and A.J.; supervision, J.P. and M.H.; funding acquisition, A.J. and M.H. All authors have read and agreed to the published version of the manuscript.

Conflicts of Interest: The authors declare that they have no known competing financial interests or personal relationships that could have appeared to influence the work reported in this paper.

References

1. Dufour, I.; Français, O. Fluidic Microsystems. *Microfluidics* **2013**, 349–388. [CrossRef]
2. Barrot, C.; Delplanque, J.-P. Liquid Microflows: Particularities and Modeling. *Microfluidics* **2013**, 89–120. [CrossRef]
3. Anduze, M.; Colin, S.; Caen, R.; Camon, H.; Conedera, V.; Do Conto, T. Analysis and testing of a fluidic vortex microdiode. *J. Micromech. Microeng.* **2001**, *11*, 108–112. [CrossRef]
4. Abgrall, P.; Gué, A.-M. Lab-on-chip technologies: Making a microfluidic network and coupling it into a complete microsystem-A review. *J. Micromech. Microeng.* **2007**, *17*, R15–R49. [CrossRef]
5. Zhou, S.; Chen, B.; Fu, E.S.; Yan, H. Computer vision meets microfluidics: A label-free method for high-throughput cell analysis. *Microsyst. Nanoeng.* **2023**, *9*, 116. [CrossRef]
6. Batista, C.C.S.; Jäger, A.; Albuquerque, B.L.; Pavlova, E.; Stepánek, P.; Giacomelli, F.C. Microfluidic-assisted synthesis of uniform polymer-stabilized silver colloids. *Colloids Surfaces A Physicochem. Eng. Asp.* **2021**, *618*, 126438. [CrossRef]
7. Albuquerque, L.J.C.; Sincari, V.; Jager, A.; Konefal, R.; Panek, J.; Cernoch, P.; Pavlova, E.; Stepanek, P.; Giacomelli, F.C.; Jager, E. Microfluidic-Assisted Engineering of Quasi-Monodisperse pH-Responsive Polymersomes toward Advanced Platforms for the Intracellular Delivery of Hydrophilic Therapeutics. *Langmuir* **2019**, *35*, 8363–8372. [CrossRef]
8. Sincari, V.; Jäger, E.; Loureiro, K.C.; Vragovic, M.; Hofmann, E.; Schlenk, M.; Filipová, M.; Rydvalová, E.; Štěpánek, P.; Hrubý, M.; et al. pH-Dependent disruption of giant polymer vesicles: A step towards biomimetic membranes. *Polym. Chem.* **2023**, *14*, 443–451. [CrossRef]
9. De Oliveira, A.M.; Jäger, E.; Jäger, A.; Stepánek, P.; Giacomelli, F.C. Physicochemical aspects behind the size of biodegradable polymeric nanoparticles: A step forward. *Colloids Surfaces A Physicochem. Eng. Asp.* **2013**, *436*, 1092–1102. [CrossRef]
10. Wang, M.; Fu, Q.; Liu, R.; Wang, C.; Li, X.; Sun, X.; Liu, G. A microfluidic manipulation platform based on droplet mixing technology. *Chem. Eng. Sci.* **2024**, *298*, 120422. [CrossRef]
11. Czerwinska, J.; Jebauer, S. Secondary slip structures in heated micro-geometries. *Int. J. Heat Mass Transf.* **2011**, *54*, 1578–1586. [CrossRef]
12. Chiarot, P.; Mrad, R.B.; Sullivan, P. A study of passive microfluidic mixers. In Proceedings of the 2004 International Conference on MEMS, NANO and Smart Systems, ICMENS 2004, Banff, AB, Canada, 25–27 August 2004; pp. 287–293.
13. Cho, Y.-K.; Han, T.-H.; Ha, S.-J.; Lee, J.-W.; Kim, J.-S.; Kim, S.-M.; Cho, M.-W. Fabrication of passive micromixer using a digital micromirror device-based maskless lithography system. *Int. J. Precis. Eng. Manuf.* **2014**, *15*, 1417–1422. [CrossRef]
14. Deshpande, M.; Gilbert, J.R.; Bardell, R.L.; Forster, F.R. Design analysis of no-moving-parts valves for micropumps. In Proceedings of the 1998 ASME International Mechanical Engineering Congress and Exposition, Anaheim, CA, USA, 15–20 November 1998; Volume 66, pp. 153–155.
15. Zhou, P.; Zhang, T.; Simon, T.; Cui, T. A Fluidic Diode and Its Application to a Valveless Micropump. In Proceedings of the 2021 IEEE 34th International Conference on Micro Electro Mechanical Systems (MEMS), Virtual, 25–29 January 2021; pp. 1005–1008. [CrossRef]
16. Okuhara, S.; Alam, M.M.A.; Takao, M.; Kinoue, Y. Performance of fluidic diode for a twin unidirectional impulse turbine. *IOP Conf. Ser. Earth Environ. Sci.* **2019**, *240*, 052011. [CrossRef]
17. De Vries, S.F.; Florea, D.; Homburg, F.G.A.; Frijns, A.J.H. Design and operation of a Tesla-type valve for pulsating heat pipes. *Int. J. Heat Mass Transf.* **2017**, *105*, 1–11. [CrossRef]
18. Thompson, S.M.; Ma, H.B.; Wilson, C. Investigation of a flat-plate oscillating heat pipe with Tesla-type check valves. *Exp. Therm. Fluid Sci.* **2011**, *35*, 1265–1273. [CrossRef]
19. Lv, Q.; Chen, M.; Sun, X.; Christensen, R.; Blue, T.; Yoder, G.; Wilson, D.; Sabharwall, P. Design of fluidic diode for a high-temperature DRACS test facility. In Proceedings of the 2013 21st International Conference on Nuclear Engineering, ICONE 2013, Chengdu, China, 29 July–2 August 2013; Volume 4.
20. Wang, B.; Su, H.; Zhang, B. Hydrodynamic cavitation as a promising route for wastewater treatment–A review. *Chem. Eng. J.* **2021**, *412*, 128685. [CrossRef]

21. Bhandari, V.M.; Sorokhaibam, L.G.; Ranade, V.V. Industrial wastewater treatment for fertilizer industry—A case study. *Desalin. Water Treat.* **2016**, *57*, 27934–27944. [CrossRef]
22. Patil, P.B.; Bhandari, V.M.; Ranade, V.V. Improving efficiency for removal of ammoniacal nitrogen from wastewaters using hydrodynamic cavitation. *Ultrason. Sonochem.* **2021**, *70*, 105306. [CrossRef]
23. Kotowski, A.; Wójtowicz, P. Analysis of hydraulic parameters of cylindrical vortex regulators. *Environ. Prot. Eng.* **2008**, *34*, 43–56.
24. Ochowiak, M.; Włodarczak, S.; Matuszak, M.; Krupińska, A.; Markowska, M. Flow Regulators-Design, Tests and Applications. In *Practical Aspects of Chemical Engineering: Selected Contributions from PAIC 2019*; Springer: Berlin/Heidelberg, Germany, 2020; pp. 261–270. [CrossRef]
25. Jain, P.; Bhandari, V.M.; Balapure, K.; Jena, J.; Ranade, V.V.; Killedar, D.J. Hydrodynamic cavitation using vortex diode: An efficient approach for elimination of pathogenic bacteria from water. *J. Environ. Manag.* **2019**, *242*, 210–219. [CrossRef]
26. Suryawanshi, N.B.; Bhandari, V.M.; Sorokhaibam, L.G.; Ranade, V.V. A Non-catalytic Deep Desulphurization Process using Hydrodynamic Cavitation. *Sci. Rep.* **2016**, *6*, 33021. [CrossRef] [PubMed]
27. Suryawanshi, P.G.; Bhandari, V.M.; Sorokhaibam, L.G.; Ruparelia, J.P.; Ranade, V.V. Solvent degradation studies using hydrodynamic cavitation. *Environ. Prog. Sustain. Energy* **2018**, *37*, 295–304. [CrossRef]
28. Suryawanshi, N.B.; Bhandari, V.M.; Sorokhaibam, L.G.; Ranade, V.V. Developing techno-economically sustainable methodologies for deep desulfurization using hydrodynamic cavitation. *Fuel* **2017**, *210*, 482–490. [CrossRef]
29. Sarvothaman, V.P.; Kulkarni, S.R.; Subburaj, J.; Hariharan, S.L.; Velisoju, V.K.; Castaño, P.; Guida, P.; Prabhudharwadkar, D.M.; Roberts, W.L. Evaluating performance of vortex-diode based hydrodynamic cavitation device scale and pressure drop using coumarin dosimetry. *Chem. Eng. J.* **2024**, *481*, 148593. [CrossRef]
30. Simpson, A.; Ranade, V.V. 110th Anniversary: Comparison of Cavitation Devices Based on Linear and Swirling Flows: Hydrodynamic Characteristics. *Ind. Eng. Chem. Res.* **2019**, *58*, 14488–14509. [CrossRef]
31. Qu, S.-X.; Wu, Y.-H.; He, Z.-Z.; Chen, K. Surrogate Fluid Experimental Study and CFD Simulation on the Hydraulic Characteristics of Vortex Diode. *Nucl. Sci. Eng.* **2018**, *189*, 282–289. [CrossRef]
32. Doddamani, H.; Abdus, S.; Manabu, T.; Shinya, O.; Ashraful Alam, M.M. Effect of Fluidic Diode on Performance of Unidirectional Impulse Turbine. *J. Therm. Sci.* **2024**, *33*, 807–814. [CrossRef]
33. Dudhgaonkar, P.V.; Jayashankar, V.; Jalihal, P.; Kedarnath, S.; Setoguchi, T.; Takao, M.; Nagata, S.; Toyota, K. Fluidic Components for Oscillating Water Column Based Wave Energy Plants. In Proceedings of the Fluids Engineering Division Summer Meeting, Hamamatsu, Japan, 24–29 July 2011; pp. 1979–1983. [CrossRef]
34. Hithaish, D.; Das, T.K.; Takao, M.; Samad, A. Design Optimization of a Fluidic Diode for a Wave Energy Converter via Artificial Intelligence-Based Technique. *Arab. J. Sci. Eng.* **2023**, *48*, 11407–11423. [CrossRef]
35. Kerikous, E.; Hithaish, D.; Samad, A.; Hoerner, S.; Thévenin, D. Performance Enhancement of Fluidic Diode for a Wave Energy System through Genetic Algorithm. *Proc. Eur. Wave Tidal Energy Conf.* **2023**, *15*, 1–6. [CrossRef]
36. Cao, Z.; Zhao, T.; Wang, Y.; Wang, H.; Zhai, C.; Lv, W. Novel fluid diode plate for use within ventilation system based on Tesla structure. *Build. Environ.* **2020**, *185*, 107257. [CrossRef]
37. Adams, M.L.; Johnston, M.L.; Scherer, A.; Quake, S.R. Polydimethylsiloxane based microfluidic diode. *J. Micromechanics Microengineering* **2005**, *15*, 1517. [CrossRef]
38. Kulkarni, A.A.; Ranade, V.V.; Rajeev, R.; Koganti, S.B. Pressure drop across vortex diodes: Experiments and design guidelines. *Chem. Eng. Sci.* **2009**, *64*, 1285–1292. [CrossRef]
39. Kulkarni, A.A.; Ranade, V.V.; Rajeev, R.; Koganti, S.B. CFD simulation of flow in vortex diodes. *AIChE J.* **2008**, *54*, 1139–1152. [CrossRef]
40. Saito, M.; Arai, F.; Yamanishi, Y.; Sakuma, S. Spatiotemporally controlled microvortices provide advanced microfluidic components. *Proc. Natl. Acad. Sci. USA* **2024**, *121*, e2306182121. [CrossRef]
41. Chen, C.-N.; Zhou, L.-J.; Jiao, L.; Liu, J.-T.; Wang, L.-Q. Numerical simulation of axial port structure on vortex diode performance. *J. Eng. Thermophys.* **2010**, *31*, 185–188.
42. Jiao, L.; Chen, C.-N.; Wu, C.-J.; Liu, J.-T.; Wang, L.-Q. Numerical simulation of tangential port on vortex diode performance. *J. Eng. Thermophys.* **2011**, *32*, 415–418.
43. Jiao, L.; Chen, C.-N.; Liu, S.-G.; Yin, J.-L.; Sun, Q.-J.; Wang, L.-Q. Numerical simulation of three-dimensional strong rotational flow in vortex diode. *J. Eng. Thermophys.* **2011**, *32*, 1855–1858.
44. Cao, Y.; Wu, Y.; Lin, C.; He, Z.; Chen, K. Numerical simulation of the performance of vortex diodes with chamfered vortex chambers. *Nuclear Tech.* **2015**, *38*, 010602. [CrossRef]
45. Jiao, L.; Wu, C.-J.; Chen, C.-N.; Yin, J.-L.; Liu, J.-T.; Wang, L.-Q. Numerical simulation of cavitation performance for vortex diode. *J. Eng. Thermophys.* **2012**, *33*, 1519–1522.
46. Jiao, L.; Zhang, P.P.; Chen, C.N.; Yin, J.L.; Wang, L.Q. Experimental study on the cavitation of vortex diode based on CFD. In Proceedings of the IOP Conference Series: Earth and Environmental Science, Beijing, China, 19–23 August 2012; Volume 15.
47. Wang, J.; Wei, Z.; Gou, J.; Xiao, Q.; Li, S.; Li, Y. CFD numerical simulation of water hammer in a vortex diode. In Proceedings of the 2018 26th International Conference on Nuclear Engineering, ICONE 2018, London, UK, 22–26 July 2018; Volume 8.
48. Liu, X.; Zhang, H.; Han, X.; Zhao, L. Simulation of backward facing step flow at the outlet of micro-channel and optimal design of amperometric detection chip. In Proceedings of the 8th Annual IEEE International Conference on Nano/Micro Engineered and Molecular Systems, Suzhou, China, 7–10 April 2013; pp. 578–581. [CrossRef]

49. Fouladi, K.; Czupryna, J. CFD-based optimization of micro vortex diodes. *J. Appl. Fluid Mech.* **2018**, *11*, 1231–1237. [CrossRef]
50. Wilcox, D.C. *Turbulence Modeling for CFD*, 3rd ed.; DCW Industries: La Cañada, CA, USA, 2006; ISBN 1928729088/978-1928729082.
51. Versteeg, H.K.; Malalasekera, W. *An Introduction to Computational Fluid Dynamics: The Finite Volume Method*, 5th ed.; Longman Group Ltd.: Harlow, UK, 1995; ISBN 0-582-21884-5.
52. Pope, S.B. *Turbulent Flows*; Cambridge University Press: Cambridge, UK, 2000; ISBN 9780521598866. [CrossRef]